Numerical characterisation of noise generated by a distributed-propulsion propeller

Sidharath Sharma*,Guangyuan Huang†,Stephen Ambrose‡ and Richard Jefferson-Loveday§
Gas Turbine and Transmissions Research Centre (G2TRC), University of Nottingham, Nottingham, NG7 2TU

The shift towards sustainable and eco-friendly future of aviation is further catalysed by the aggressive targets set by administrative and industrial stakeholders. It has emerged as one of the solutions with the potential to increase overall efficiency and improve noise emissions. This paper characterises the flow and acoustic field associated with a DEP propeller. A hybrid methodology using scale-resolving turbulence formulation and an acoustic analogy is used to predict aerodynamic noise generation and acoustic wave propagation to the far-field for an isolated DEP propeller. The numerical predictions are observed to be in reasonable agreement with the measured values for both aerodynamic and aero-acoustic attributes. The sensitivity of far-field acoustic spectra to the integration surface is also presented. The results are further analysed to identify dominant noise sources in the system including propeller and wake flows.

I. Nomenclature

ρ	=	density
RANS	=	Reynolds-averaged Navier-Stokes
LES	=	Large eddy simulation
WALE	=	Wall-adopted local eddy-viscosity
DEP	=	Distributed electric propulsion

II. Introduction

Sustainable aviation and protection of the environment by decarbonising and slashing emissions form a critical part of the European vision for the aviation industry as specified in Flightpath 2050 [1]. The objectives are in line with the air transport action group's (ATAG) targets [2] to tackle climate change impact and includes reductions relative to a standard new aircraft in 2000 as:

- Reduction in NO_x emissions by 90%
- Reduction in CO_2 emission per passenger kilometre by 75%
- 65% reduction in the perceived noise emission of a flying aircraft

Distributed propulsion approaches are being researched [3] as a means to achieve this vision. The approach of using multiple propulsion units spread across the vehicle for providing thrust in such a way that it improves the performance and/or capabilities of the system is a describing feature of the distributed propulsion. The system in which thrust is obtained by electrical motor driven propulsors connected to electrical power sources via transmission lines is called distributed electric propulsion (DEP). DEP concepts have shown promise to achieve the aforementioned aggressive targets by enabling opportunities for higher overall efficiency and improved noise emissions [3], specifically suitable for regional routes.

The source of electrical power i.e. power generation and/or energy storage devices and the propulsion devices producing thrust are not mechanically connected. This decoupling opens up opportunities in addition to the benefits of incorporating efficient and compact electrical machines. These benefits include individual optimisation of power sources and propulsors in terms of number, location and size. Furthermore, there is a huge potential in drag reduction and efficiency improvement with the DEP concept [4] by altering wing sizes, vertical tail-plane and high-lift systems.

*Research Fellow, Department of Engineering, sidharath.sharma@nottingham.ac.uk
†Research Fellow, Department of Engineering, guangyuan.huang@nottingham.ac.uk
‡Assistant Professor, Department of Engineering, stephen.ambrose3@nottingham.ac.uk
§Associate Professor, Department of Engineering, richard.jefferson-loveday@nottingham.ac.uk

Among critical design considerations for a DEP configuration that needs in-depth examination is the noise generated by such a system. The understanding of noise generation mechanisms necessitates high-fidelity models, and consequently, can enable better and quieter designs. This exploration is initialised by investigating the aerodynamic noise generated by an isolated DEP propeller.

A propeller system generates aerodynamic noise in both tonal or discrete and broadband frequencies. The mechanisms of discrete-frequency noise generation are deterministic components of [5, 6] thickness noise, loading noise (non-impulsive loading noise, blade-vortex interaction noise), high-speed impulsive noise and quadrupole noise. Broadband noise is caused by non-deterministic sources of loading noise such as turbulence ingestion noise, self-noise (trailing edge noise, blade-wake interaction noise, tip vortex formation and laminar vortex shedding). Although noise generation mechanisms in classical propeller based applications such as helicopters are well researched in the literature, noise generation in DEP propellers could be significantly different due to deviations in the size and operational parameters (rotational speed, Reynolds number, Mach number). For instance, Mach numbers for helicopter propeller tips are usually [7] between $0.7 \leq M_{tip} \leq 0.8$ while DEP propellers are in the range of $0.1 \leq M_{tip} \leq 0.2$. This puts the acoustic signature of DEP propellers closer to small unmanned aerial vehicles (UAVs) propellers than the classical helicopter propellers. Furthermore, the impact of the wake in the noise generation by the complete system for the hovering regime is expected to be different from the forward-flight regime. Pertinent literature on noise generation in the UAV's is reviewed in this work.

Diaz and Yoon [8], Perez and Lopez [9], Zawodny et al. [10], Afari et al. [11] and Mankbadi et al. [7] numerically investigated aerodynamic and acoustic aspects of small commercial UAVs. Diaz and Yoon [8] used a higher-order accurate code with detached eddy simulation (DES) based turbulence formulation to model aerodynamic aspects of single rotor and multi-rotor commercial drones while the acoustic aspects were not deliberated. Perez and Lopez [9] also investigated flow field of a small UAV without solving for the acoustic parameters. Zawodny et al. [10] used unsteady Reynolds-averaged Navier-Stokes (RANS) coupled with the Ffowcs-Williams and Hawkings (FW-H) acoustic analogy to study broadband noise propagation for a small UAV while Afari et al. [11] and Mankbadi et al. [7] employed the DES turbulence formulation along with the FW-H formulation to investigate the propagation of both tonal and broadband noise generated by a small UAV to the far-field. Several experimental campaigns to acoustically characterise small UAVs include the work of Lu et al. [12] and Intaratep et al. [13] while aerodynamic interaction between the propellers of a DEP system is explored by Vries et al. [14].

The current work focuses on computing flow field and corresponding acoustic propagation with an intent to understand the acoustic aspects of a DEP concept. The experimental campaign to measure acoustic characteristics of an isolated propeller is presented in Sec. III followed by a brief discussion on the adopted hybrid computational aero-acoustic (CAA) methodology for modelling in Sec. IV. The details of computational model and obtained results are presented in Sec. V and Sec. VI respectively. Finally, the outcome of this work is summarised in Sec. VII.

III. Experimental Measurements

The aerodynamic and acoustic performance of an isolated propeller is experimentally characterised by measuring aerodynamic thrust and far-field noise. The measurements are performed by the team in the University of Bristol in their large aeroacoustic facility which is a closed-circuit, open-jet aeroacoustic wind tunnel housed in an anechoic chamber of dimensions $7.9\,\text{m} \times 5.0\,\text{m} \times 4.6\,\text{m}$ fully anechoic down to 160 Hz. The contraction nozzle used in the wind tunnel is of dimensions $0.5\,\text{m} \times 0.775\,\text{m}$. The wind tunnel and its components are appropriately designed to yield a sufficiently low background noise for accurate far-field measurements. Further details on the performance characteristics of the wind tunnel are available in Mayer et al. [15, 16].

The propeller and brushless electric motor are coupled via an adapter in the test rig. A load cell and speed controller are also integrated in the test rig as illustrated in Fig. 1. The speed and thermal characteristics of the motor driving the propeller are optimised for the operational range of the propeller. The rig and its supporting structures are housed in a hub designed aerodynamically to minimise interference with the flow. Furthermore, the rig is securely connected to the floor to minimise and avoid mechanical vibrations during its operation. The propeller rig was located along the axis of the nozzle approximately 600 mm (dx) away from the nozzle exit. This ensures uniformity of the incoming flow on the propeller by staying within the jet core [15] and the acoustic reflections from the lip of the nozzle are also minimised. Furthermore, acoustic foam is used to cover the potential sources of the reflective noise. The operation of a $\sim 0.23\,\text{m}$ (9 inch) diameter propeller with pitch to diameter ratio (P/D) of 1 is investigated under an inflow velocity of 12 m/s with a turbulent intensity of 4.9 % and a rotational speed of 6500 rpm.

The aerodynamic performance of the propeller is measured as thrust using multi-axis force transducers i.e. calibrated

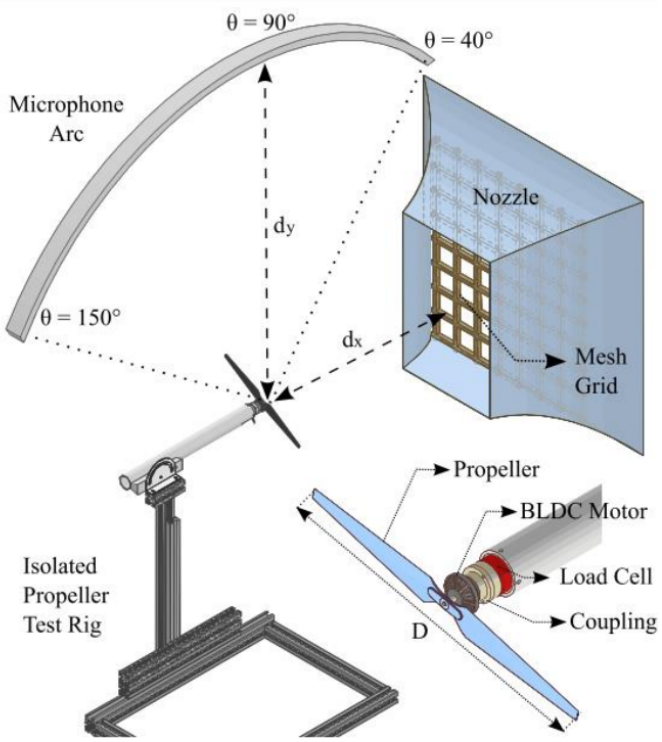

Fig. 1 Schematic of the isolated propeller test rig along with the location of polar microphone array housed in the aeroacoustic facility at the University of Bristol. Adapted from Wang et al. [16].

six axis load cell (ATI F/T sensor: Mini40 [17]) mounted directly behind the motor. The far-field acoustic propagation is measured by a 1/4 inch GRAS 40PL [18] polar microphone array located above the propeller unit at a distance of 1.75 m (dy) along the nozzle axis. The array consists of 23 microphones installed on a polar arc ranging from 40 ° - 150 ° in an increment of 5 ° each as shown in Fig. 1. The signals from microphone array and load cell are acquired using NI PXIe-1082 [19] system with a sampling rate of ~ 65.536 kHz. The signals are acquired for a total duration of 16 s to ensure statistically sufficient data length.

IV. Numerical Methodology

Aero-acoustic phenomena can be completely described by the compressible Navier-Stokes (NS) equations. The numerical methods used to solve aerodynamic problems can also resolve the generation of aerodynamic sound, the interaction between the aerodynamic and acoustic fluctuating fields and the propagation of acoustic waves. This computational approach is referred to as a direct method. However, the characteristics of aero-acoustic problems (such as disparity in energy and length scales, non-linearities) are significantly different from typical aerodynamic problems [20] due to the distinct nature of the acoustic and flow variables. These distinctions limit the use of the direct approach for industrial aero-acoustic problems as being computationally intractable and inefficient. Furthermore, the differences in the physics of noise generation and noise propagation justify the decomposition of the problem into different computational domains, which can then be resolved by different numerical methods. This approach is termed as a hybrid method to model aero-acoustic problems [21]. Figure 2 illustrates the decomposition of the computational domain in three different regions viz. source, acoustic near-field and acoustic far-field region. The former region accounts for the aerodynamic sound generation while the latter two are concerned about the propagation of acoustic waves. This decomposition of the computational domain in a hybrid approach, by default assumes the non-interference between different regions i.e. acoustic waves in the propagation region do not have any bearing on the noise generation mechanisms in the source region. Therefore, the primary application of the hybrid approach is for problems with the flow at low fluctuating Mach numbers, which aptly describes the current propeller operation. Therefore, a hybrid approach to aero-acoustic modelling is selected.

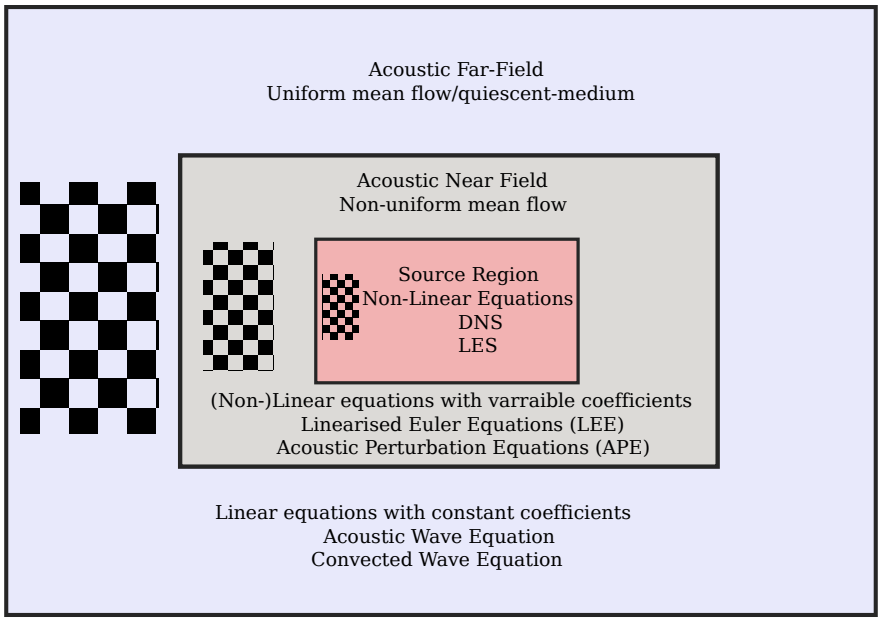

Fig. 2 Decomposition of the computational domain for a hybrid approach to aero-acoustic problems. Adapted from Rubio [22]

.

In essence, a methodology for aero-acoustic analysis requires the appropriate selection of the means to solve the aerodynamic equations and propagation equations with optimal numerical and coupling techniques. The reliability of the acoustic predictions made by using hybrid approaches primarily depend on accurate noise source modelling. This necessitates employing high fidelity scale resolving turbulence formulations. Ideally, the complete resolution of the aerodynamic scales by the means of direct numerical simulation (DNS) should be used but it is not computationally feasible. Alternatively, part of the turbulent spectrum resolved by the means of scale-resolving simulations can be used for aero-acoustic computations by hypothesising the efficient radiation of the noise by larger scales relative to smaller scales. In this work, large eddy simulations (LES) is used to model the source region.

The coupling between source and propagation region is critical for an aero-acoustic analysis and is performed in this work by using equivalent sources coupling strategy. This is based on the theory of the acoustic analogy wherein the NS equations are reformulated to yield acoustic propagation and equivalent acoustic sources. For a flow solution $\mathbf{q}$ satisfying compressible flow equations $\aleph(\mathbf{q}) = 0$, an acoustic analogy can be formulated by rearranging $\aleph(\mathbf{q}) = 0$ into $L\mathbf{q} = S(\mathbf{q})$ where L is a wave propagation operator and $S(\mathbf{q})$ is its corresponding equivalent sound source [23]. The intent of this reformulation is the inversion of L to provide $\mathbf{q}$ in the far-field where it only contains acoustic information. For rotor noise, the FW-H approach has been extensively [5, 24] used in the literature.

Ffowcs-Williams and Hawkings [25] extended the work of Curle [26] and Lighthill [27] to develop a general analogy incorporating the effect of surfaces in arbitrary motion. The source region variables are assumed to be of purely aerodynamic nature. The integral formulation of the FW-H equation is derived using the free-space Green's function. In applying the FW-H equation, the volume quadrupole noise is negligible at low Mach numbers but becomes important at transonic and supersonic Mach numbers. The explicit evaluation of quadrupole sources can be avoided by applying the FW-H equation on a fictitious, permeable surface instead of the physical surface. This would lead to the inclusion of the effect of the volume sources within the surface in the surface source terms. The replacement of solid boundaries by a permeable stationary surface yields an alternative formulation of FW-H [25] analogy. A permeable stationary surface S described by $g = 0$ will yield the following wave equation [28]:

$$\frac{\partial^2 \rho}{\partial t^2} - {c_0}^2 \nabla^2 \rho = \frac{\partial^2}{\partial x_i \partial x_j} \left(T_{ij} H(g) \right) - \frac{\partial}{\partial x_i} (\rho u_i u_n \delta(g)) + \frac{\partial}{\partial t} (\rho u_n \delta(g)) \tag{1}$$

where $H(g)$ represents Heaviside function with value 0 for $g < 0$ (interior domain) and 1 for $g > 0$ (exterior domain). The velocity of fluid normal to the surface is represented by u_n and the intensity of local force on the surface is assumed

to be 0. Similar formulations are also derived for the moving surfaces [5, 29] too. Furthermore, the permeable F-WH formulation allows to include sources placed outside the permeable surface, a surface located in the non-linear source region can be used in this approach. Placement of an appropriate integral surface can be tricky and a potential source of error. Therefore, the permeable F-WH formulation is used in this work to model the propagation of acoustic waves to far-field and the various locations of integral surfaces are investigated.

In near-field region, the computed pressure fluctuations are recorded using various virtual probes while fluctuations in the far-field are computed at the locations similar to that of the polar microphone using FW-H. The measured and computed pressure traces are processed using Welch's overlapped segmented averaging procedure [30]. The data blocks are tapered using Hanning functions with a 50% overlap to compute power spectral density (dB/Hz).

V. Computational model

The propeller is designed and manufactured by the industrial partner Mejzlik [31]. The Clark-Y aerofoil section is used with a constant-pitch design approach for selected pitch-to-diameter (P/D) ratio that can be tested in the wind tunnel. The computational domain (see Fig. 3) is extended to 7D in the streamwise direction with 2D upstream and 4D in the crossflow directions. The computational domain is meshed as poly-hexcore [32] control volume generated in the Fluent Meshing [33]. In this meshing configuration, octree hexahedron elements in the bulk region are connected to isotropic poly-prisms used to model (propeller) walls and the boundary layer. This arrangement is expected to yield lower cell count and thereby, speeding up the model solution [32] as compared to conventional hexcore meshes. The grid is shown in Fig. 3.

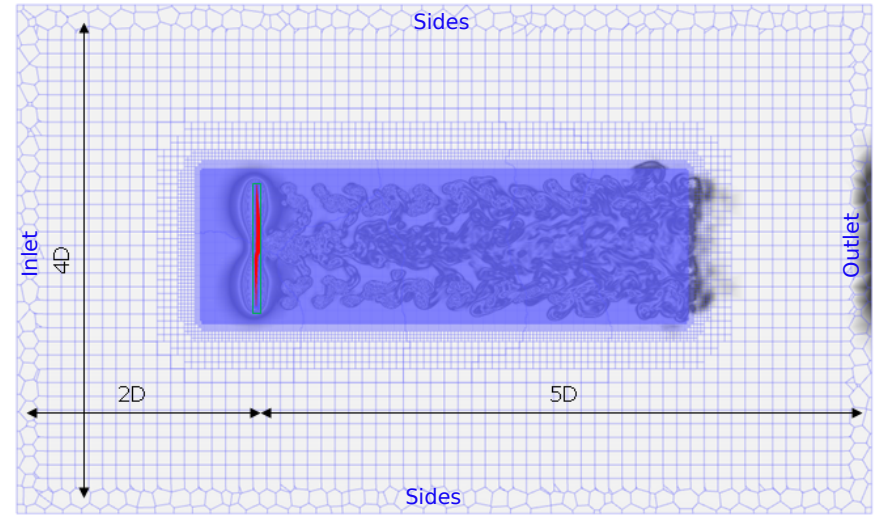

Fig. 3 Axial cross-section of the computational domain specifying dimensions and boundaries.

Ansys Fluent [34] is employed for solving the governing aerodynamic equations as well as acoustic wave propagation using the FW-H implementation. The fluid is assumed to be air behaving as a perfect gas with the ideal gas law modelling the fluid behaviour and Sutherland's law approximating the dynamic viscosity. The propeller motion is modelled using the rigid body motion approach, also known as sliding mesh in which the mesh actually rotates every time step at the interface. A non-reflecting boundary condition of steady pressure far-field [34] specifying free-stream Mach number and static pressure is used for the inlet, outlet and the sides of computational domain. A numerical configuration with sponge layer [34] along with pressure far-field boundary condition was also investigated, and yielded similar results. Therefore, only non-reflecting pressure far-field boundary condition was selected for this work. The value of Mach number is computed based on the inflow velocity used in the experimental campaign. The model uses 1% turbulent intensity at the inlet. The propeller walls are modelled as smooth with adiabatic and no-slip boundary condition.

In this work, LES turbulence formulation with the Wall-Adopted Local Eddy-viscosity (WALE) [35] model is used with an intent to resolve the flow till the viscous sublayer assuming the wall resolution is sufficient. The WALE-LES uses an algebraic local eddy viscosity based subgrid model to dissipate eddies in viscous sublayer and near wall regions. This model improves upon the problem of the non-zero eddy viscosity in the laminar shear flow region observed in

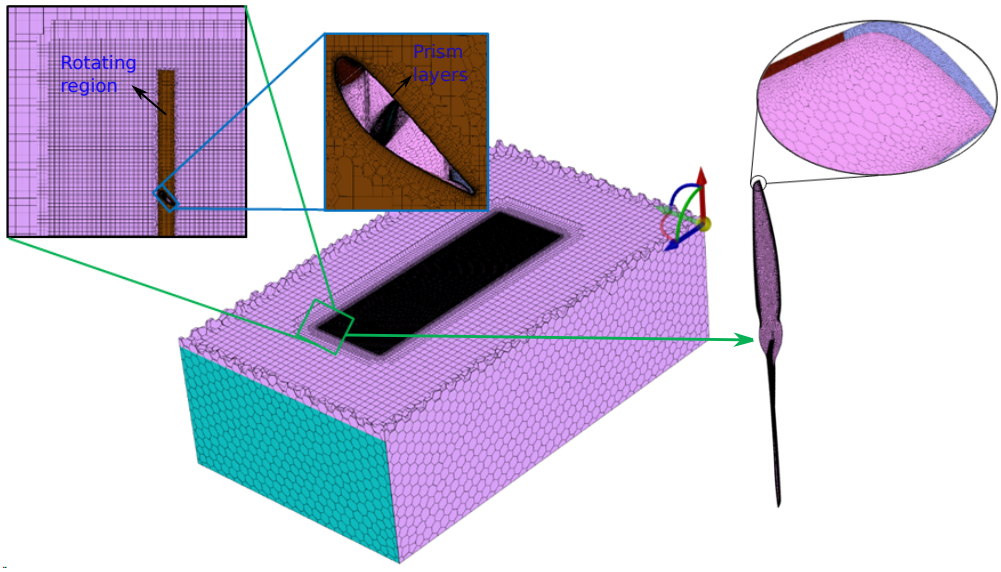

Fig. 4 View of the computational domain, highlighting a slice of the fluid mesh and including the rotor surface mesh and wake region refinement. Detail views show rotating region and the boundary layer inflation.

the Smagorinsky model [35]. The convective terms are discretised using bounded central difference scheme that is a combination of the second-order accurate central difference scheme and the first-order upwind scheme to maintain the boundedness of the solution. An implicit, second-order accurate scheme implemented in ANSYS Fluent [34] is used for temporal discretisation. The near-wall grid in terms of the height of the first cell is selected to resolve boundary layer flow, specifically the viscous sublayer, by achieving a value of $y+$ less than unity. The contours of y+ value distribution at the propeller surface is shown in Fig. 5.The boundary layer region is modelled using 20 prism layers.

Two mesh configurations viz. coarse and fine grids are investigated in this work. With the similar near-wall grid, the coarse grid consists of approximately 6 million cells and the fine grid consists of approximately 22 million cells. The solution is advanced with a physical time step of 5×10^{-5} s corresponding to 2 ° propeller rotation for the coarse grid case and 10^{-5} s corresponding to 0.39 ° propeller rotation for the fine grid case with up to 50 dual-time sub-iterations yielding a 3 orders of magnitude drop in sub-iteration residual.

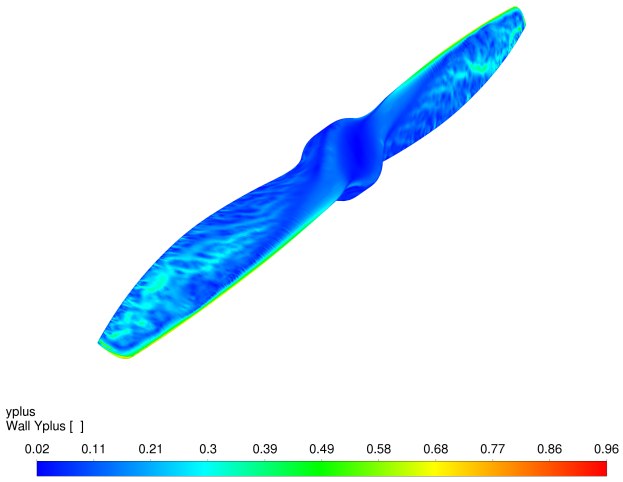

Fig. 5 4. Contours of y+ across the propeller surface.

VI. Computational Results

The credibility of the numerical predictions are ascertained by comparison with the experimental results. The predicted aerodynamic thrust as well as sound pressure levels in the far-field are compared with the measured values. This validation of the numerical model as well as further insights are presented in the upcoming section.

A. Aerodynamic Characteristics

The forward axial force predicted by the fine-grid numerical configuration is shown in Fig. 6. The mean values of the predicted thrust generated by the propeller in both numerical configurations along with the relative deviation from experimentally measured value are presented in Tab. 1. The mean thrust values are slightly over-predicted and are observed to be in good agreement with the experimental measurement.

Table 1 Mean thrust predicted numerically are compared with the experimental measurement.

Case	Mean Thrust [N]		Relative Deviation
	Numerical	Experimental	
Coarse mesh case	3.21	3.20	0.3
Fine mesh case	3.22		0.6

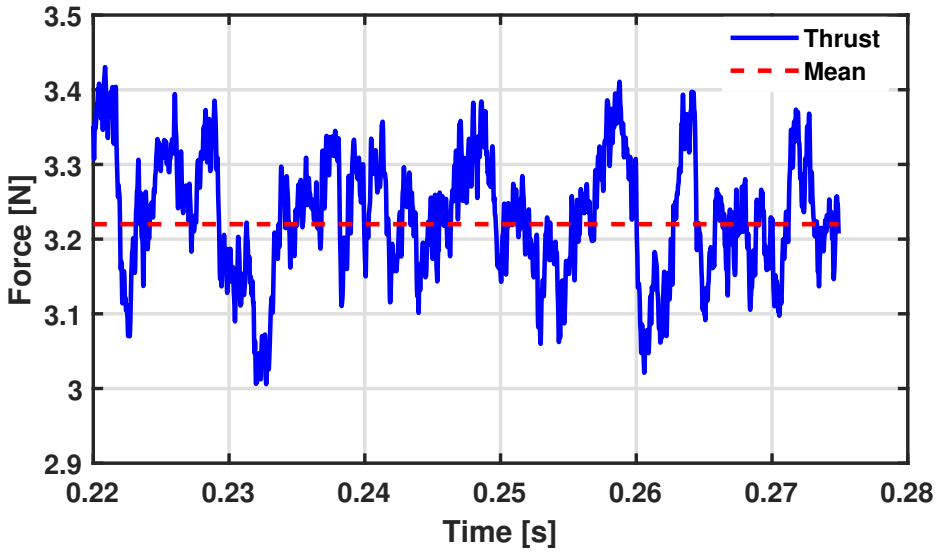

Fig. 6 Thrust generated by the propeller. Instantaneous thrust value (blue) along with the mean value (red) over the time are presented.

The contours of velocity and vorticity magnitude on the axial plane for the fine-grid configuration are presented in Fig. 7. The smaller eddies are observed in the wake and agree with the results presented by Diaz and Yoon [8]. To further the visual inspection of the wake flow, a shadowgraph defined as the magnitude of $\nabla\rho/\rho$ has been plotted at the axial plane in Fig. 8 (left). The behaviour of the wake flow can be seen as the entrainment of swirling jet with the downstream decay. In case of multiple propellers, this wake interactions is expected to be a significant quadrupole acoustic source. Fig. 8 (right) shows the iso-surfaces of Q-criterion coloured by the vorticity magnitude emphasising the swirling behaviour of the wake flow.

B. Near-Field Characteristics

Near-field spectra for the three points as shown in Fig. 9). The blade passing frequency (~ 216.67 Hz) is observed in the spectra of all three locations. A broadband noise feature is also observed in the spectra of all three point in the range

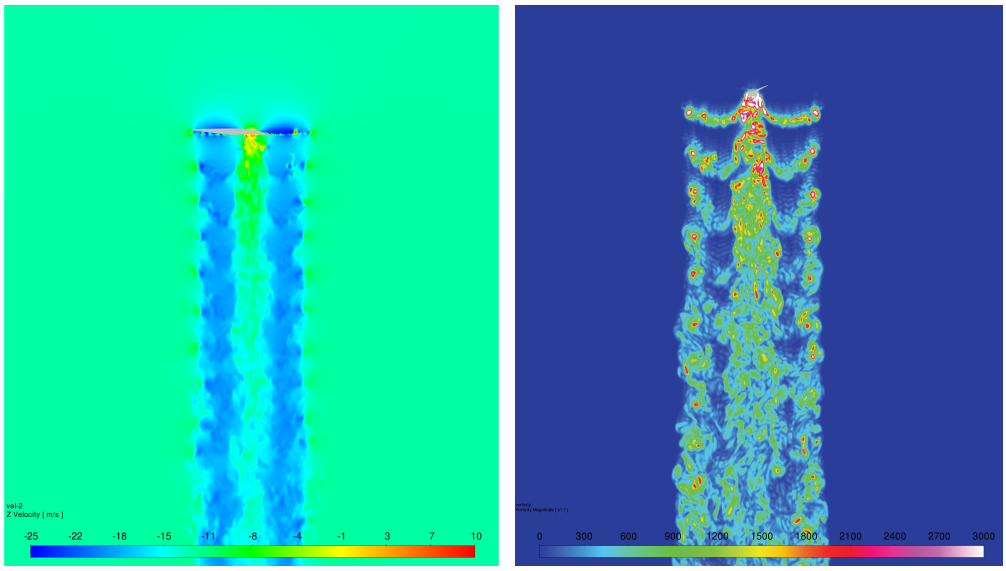

Fig. 7 Instantaneous contours of axial velocity magnitude (left) and vorticity magnitude (right) on the axial plane.

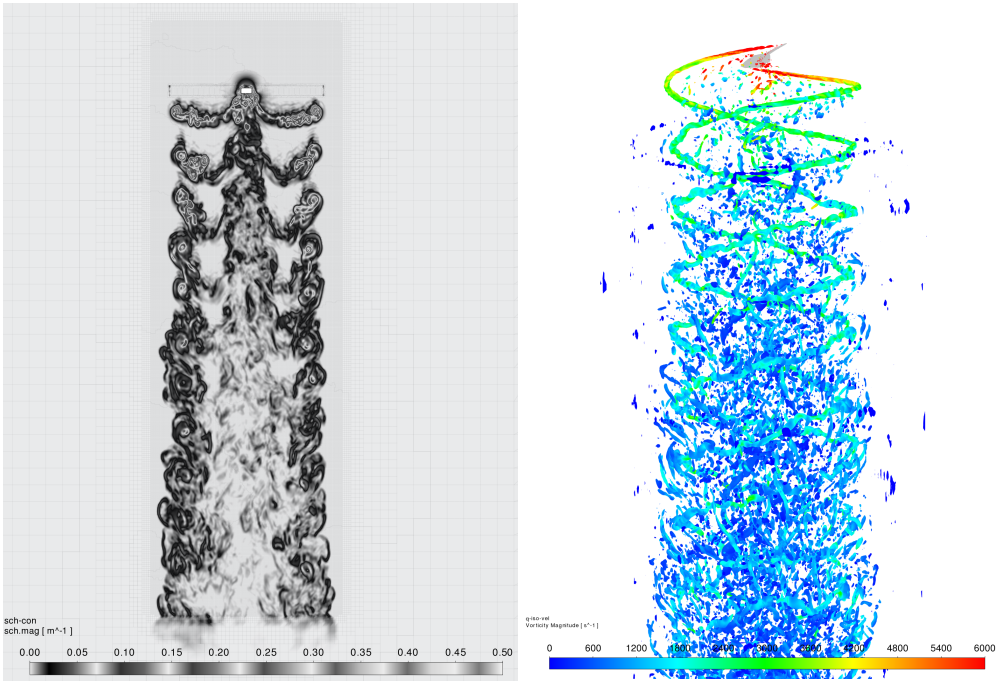

Fig. 8 Instantaneous shadowgraph contours (left) at the axial plane and iso-surfaces of Q-criterion (right) coloured by the magnitude of vorticity.

of 2–5 kHz.

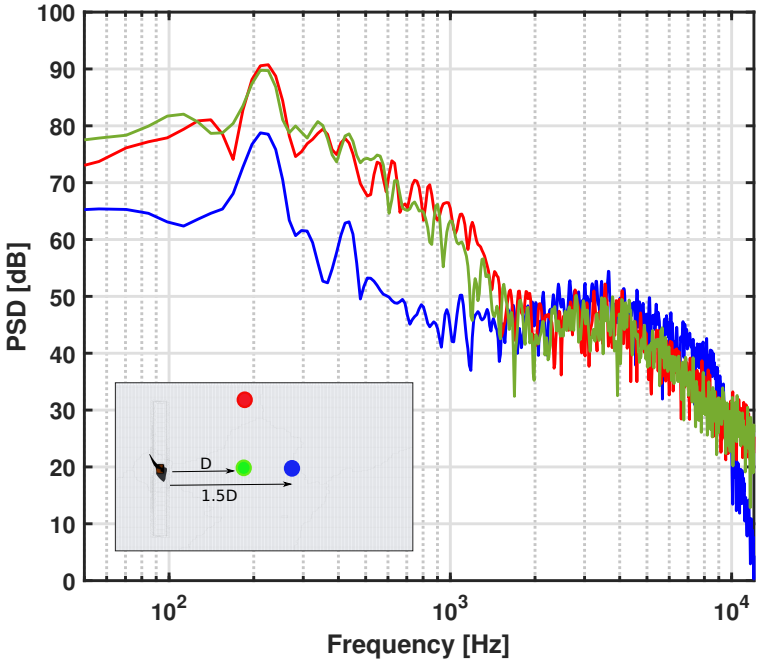

Fig. 9 Near-field pressure spectra at the specified points.

The snapshot of pressure dilatations dp/dt on the axial plane (see Fig. 10) shows both loading and thickness noise components. On the basis of visual inspection, the loading noise component appears to be stronger than the thickness noise component for the current case.

C. Far-Field Characteristics

The far-field aeroacoustic noise measurements and predictions of the isolated propeller are discussed in this section. Acoustic FW-H analogy is used in this work to predict far-field acoustic characteristics wherein both solid and permeable surfaces are investigated. Acoustic monopoles and dipoles, also known as thickness and loading noise sources respectively are included in the (solid) surface distributions while quadrupole term is neglected. The impact of volume or quadrupole term is incorporated using the permeable surface formulation. Various FW-H surfaces that includes propeller surface (solid), an envelope around the propeller wake (permeable) and an envelope around the propeller (permeable) investigated in the work are shown in Fig. 11. It is worth pointing out that the near-blade envelope (blue dashed line in Fig. 11) is only investigated for the fine mesh case.

The sound pressure level measured at microphone 11 of the polar array representing an above-plane observer is compared with the numerical results in Fig. 12. The numerical results of both coarse and fine mesh cases using propeller surface and wake envelope as FW-H surface are compared with the measured values. It is important to point out that the experimental data presented in Fig. 12 corresponds to the propeller operating at 7000 rpm with the inflow velocity of 10 m/s. Due to the lack of availability of the exact operating configuration used in the numerical modelling i.e. 6500 rpm and 12 m/s, closest acoustic measurement configuration is chosen to validate the numerical predictions. The tonal features i.e. blade pass and its harmonics are observed in the predictions from the coarse mesh configuration while the spectra is seen to decay rapidly as compared to experimental results. This is primarily due to the higher timestep used in the coarse configuration. The numerical results from the fine mesh configuration shows significantly better correlation with the measured values, specifically in terms of levels and the decay of spectrum at higher frequencies (< 10 kHz).

A significant increase in noise levels before the first BPF is observed in the permeable surface (wake envelope) predictions relative to the predictions using blade surface for both coarse and fine mesh cases. Blade-wake interactions and leading edge interactions are known to impact at the lower frequencies [36], and therefore, it can be inferred that the leading-edge interactions are better resolved by using wake envelope. It is also interesting to observe that the decay of the spectra at higher frequencies is better captured by the predictions from propeller surface as compared

Fig. 10 Snapshot of pressure dilatation dp/dt on the axial plane.

to the wake envelope. The shape and amplitude of tonal features are in reasonable agreements for both numerical cases. The minimal differences in the broadband noise spectrum for solid and permeable surfaces implies the expected insignificance of quadrupole source for propellers with low blade-tip Mach number [37]. This being said, quadruple source is posited [7] to be significant component for multi-propeller configurations due to wake interactions. The broadband in the range of 0.7 - 1.4 kHz is not observed in the either numerical spectra. In addition to the overall levels, peak blade pass tones are under-predicted by the numerical model. This can be expected to be caused by omission of test stand, load cells, spinners and motors from the numerical model along with the surrounding walls which are shown to increase overall noise levels due to recirculation effects [36, 38]. Furthermore, the coarser frequency resolution of the numerical signal relative to measured signal also leads to the under-prediction of tonal peaks [39].

Sound pressure level of the isolated rotor at microphone 11 and 20 are compared in Fig. 13. The features in the experimentally measured spectra are reasonably captured in the numerical predictions using propeller surface of both coarse and fine mesh cases. The slight decrease in the amplitude of the BPF for microphone 20 along with the suppression of blade pass harmonic is captured in the predictions of both numerical cases. Furthermore, higher overall noise levels for microphone 20 as compared to microphone 11 are also reasonably predicted.

The impact of using solid and permeable FW-H surface for computing far-field noise propagation using coarse and fine mesh cases are presented in Fig. 14 and Fig. 15 respectively. As described previously, an increase in noise levels at lower frequencies is observed for the permeable surface implying better resolution of leading-edge interactions. However, the spectra at higher frequencies decays rapidly for permeable surfaces as compared to solid surface. The shape and amplitude of tonal features are in reasonable agreements for both solid and permeable surfaces. Additionally, near-propeller envelope used in the fine-mesh case to compute far-field noise over-predicts noise levels and the causes for this over-prediction are not understood at this time.

To understand the directivity of the propeller noise, the amplitude of sound pressure level spectra within specific frequency limits, also known as overall sound pressure level (OASPL) is computed from the root mean squared averaged of the pressure signal filtered using bandpass filter for the specified frequency range. Alternatively, the overall levels

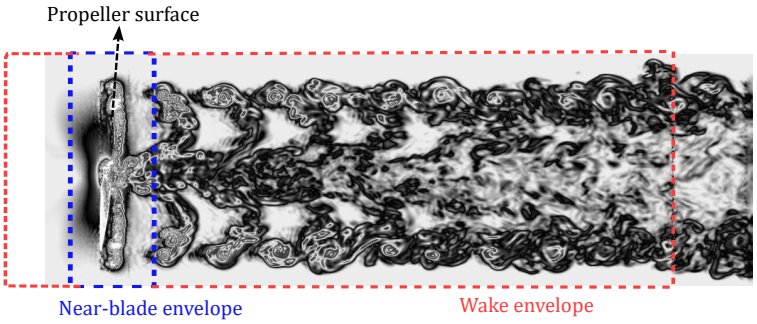

Fig. 11 Location of the FW-H integration (permeable) surface for far-field acoustic prediction. The integration surfaces includes propeller surface, envelope around the wake (red dashed line) and envelope around the propeller (blue dashed line).

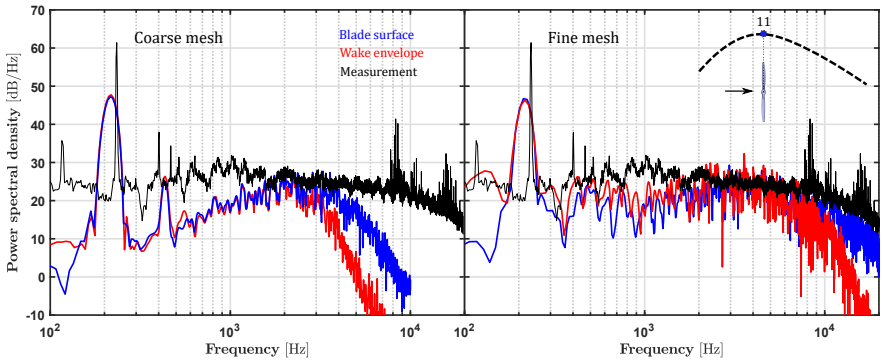

Fig. 12 Sound pressure level of the isolated rotor measured at microphone 11 (placed normal to the rotational axis) is compared to the numerical predictions from coarse (left) and fine (right) mesh.

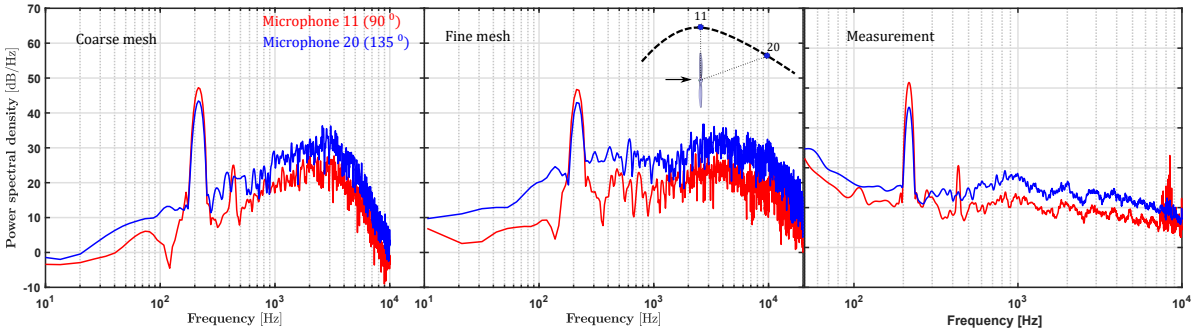

Fig. 13 Sound pressure level of the isolated rotor at microphone 11 and 20 from measurements (right), fine mesh (middle) and coarse mesh (left) are compared.

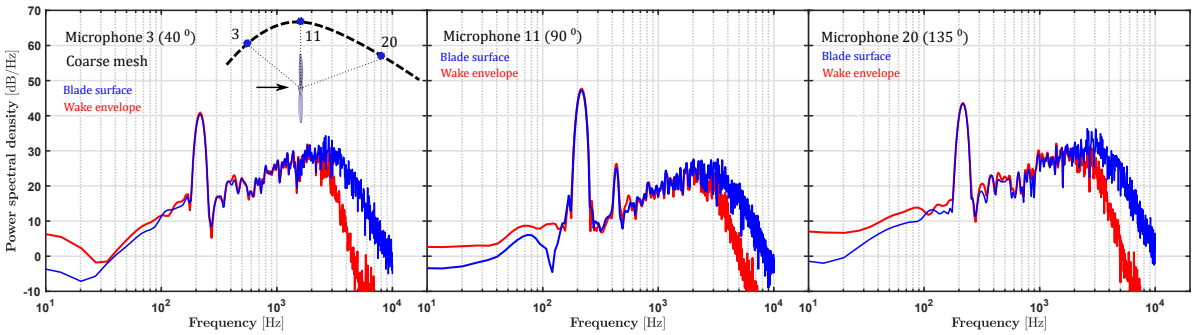

Fig. 14 Far-field acoustic calculation at three microphone locations using various FW-H surfaces for the coarse mesh case.

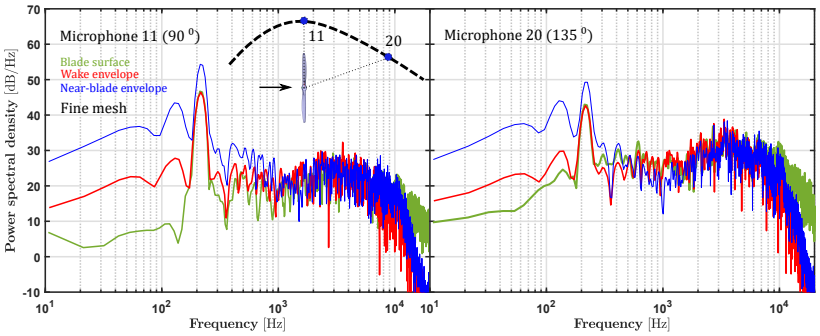

Fig. 15 Far-field acoustic calculation at two microphone locations using various FW-H surfaces for the fine mesh case.

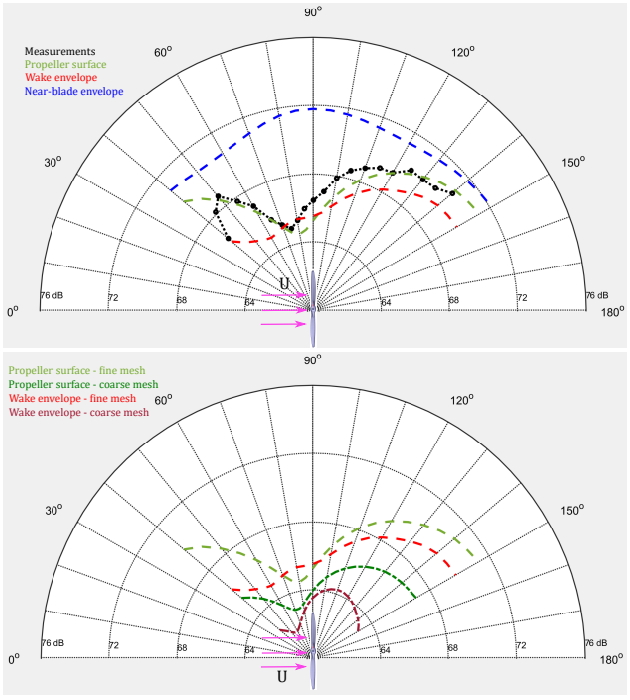

Fig. 16 Overall sound pressure level of the isolated propeller measured at the various microphones of the polar array. Numerical predictions using various FW-H surfaces for the fine mesh case (top) are compared with the experimental results (black dashed line). Furthermore, numerical predictions from the fine mesh case are compared with coarse mesh case (bottom).

between frequency bounds f_1 and f_2 can also be computed directly from the spectra by

$$\mathrm{SPL}_{f_1-f_2} = 10\log_{10}\left(\sum_{i=f_1}^{f_2} 10^{\,\mathrm{SPL}_i/10}\right) \tag{2}$$

The directivity of the propeller noise in terms of OASPL for the polar microphone array is presented in Fig. 16. The experimentally measured values are compared with the OASPL values from the far-field predictions using various FW-H surfaces for both fine and coarse mesh cases. It is worth pointing out that the power density spectrum is integrated in the frequency band of 50 Hz to 20 kHz for both experimental and fine-mesh case while 50 Hz to 10 kHz is used for coarse-case. This partly explains the significantly lower OASPL for the coarse-mesh case.

The OASPL of the experimentally measured spectra is expected to be higher than the numerical computations as the effects introduced by wall recirculation and structural components are not included. This being said, the OASPL predicted using the propeller surface are in a reasonable agreement with the measured valued except for the first two microphone of the polar array. OASPL predicted using wake-envelope permeable surface under-predicts while there is a reasonable agreement in the directivity pattern. Near-propeller envelope heavily over-predicts the OASPLS along with huge deviations in directivity pattern.

VII. Conclusion

In this paper, the aerodynamic and aeroacoustic characteristics of an isolated propeller from DEP configuration are numerically evaluated. Experimental performance values for the propeller are obtained from the testing campaign in the university of Bristol aeroacoustic wind tunnel using a polar microphone array and load cells. Computational modelling is performed using an hybrid approach wherein scale-resolving turbulence formulation is used to model flow-field and noise generation while permeable FW-H acoustic analogy is used for far-field noise propagation. Two numerical configurations i.e. coarse-mesh and fine-mesh cases are used. Aerodynamic thrust predicted by both numerical configurations are in close proximity to the measured value. The predicted acoustic spectrum using solid (propeller) surface and permeable surface (wake-envelope) demonstrated reasonable correlation to measurements in terms of tonal features for both coarse-mesh and fine-mesh cases. The overall levels and low-frequency correlation improved using wake-envelope of the fine-mesh case. Directivity results are also well correlated with the measurements using propeller surface for FW-H calculation. An inconsistency of results observed with near-propeller envelope as FW-H surface raises the further need to study placement and topology of the FW-H surface.

Acknowledgments

The project is sponsored and supported by Horizon 2020 research and innovation programme under grant agreement number 882842, for the project 'SilentProp'. The use of Sulis computing platform, which is funded by the EPSRC grant EP/T022108/1, as part of the HPC Midlands+ consortium and the access to the University of Nottingham's Augusta computing cluster is gratefully acknowledged.

References

[1] Kallas, S., and Geoghegan-Quinn, M., "Flightpath 2050: Europe's vision for aviation: Report of the high level group on aviation research," *European Union*, 2011.

[2] ATAG, "Aviation Industry Commitment to Action on Climate Change," , 2008. URL `https://www.atag.org/component/attachments/attachments.html?id=603`.

[3] Kim, H. D., Perry, A. T., and Ansell, P. J., "A review of distributed electric propulsion concepts for air vehicle technology," *2018 AIAA/IEEE Electric Aircraft Technologies Symposium (EATS)*, IEEE, 2018, pp. 1–21.

[4] Stoll, A. M., Bevirt, J., Moore, M. D., Fredericks, W. J., and Borer, N. K., "Drag reduction through distributed electric propulsion," *14th AIAA aviation technology, integration, and operations conference*, 2014, p. 2851.

[5] Brentner, K. S., and Farassat, F., "Modeling aerodynamically generated sound of helicopter rotors," *Progress in Aerospace Sciences*, Vol. 39, No. 2-3, 2003, pp. 83–120.

[6] Marte, J., and Kurtz, D., "A review of aerodynamic noise from propellers, rotors, and lift fans," *JPL Technical Report 32-7462*, 1970.

[7] Mankbadi, R. R., Afari, S. O., and Golubev, V. V., "High-Fidelity Simulations of Noise Generation in a Propeller-Driven Unmanned Aerial Vehicle," *AIAA Journal*, Vol. 59, No. 3, 2021, pp. 1020–1039.

[8] Ventura Diaz, P., and Yoon, S., "High-fidelity computational aerodynamics of multi-rotor unmanned aerial vehicles," *2018 AIAA Aerospace Sciences Meeting*, 2018, p. 1266.

[9] Lopez, O. D., Escobar, J. A., and Pérez, A. M., "Computational study of the wake of a quadcopter propeller in hover," *23rd AIAA computational fluid dynamics conference*, 2017, p. 3961.

[10] Zawodny, N. S., Boyd Jr, D. D., and Burley, C. L., "Acoustic characterization and prediction of representative, small-scale rotary-wing unmanned aircraft system components," *American Helicopter Society (AHS) Annual Forum*, 2016.

[11] Afari, S. O., Mankbadi, R. R., and Golubev, V. V., "Towards High-Fidelity Analysis of Noise Radiation and Control of Propeller-Driven UAV," *25th AIAA/CEAS Aeroacoustics Conference*, 2019, p. 2632.

[12] Lu, Z., Debiasi, M., and Khoo, B. C., "Acoustic characteristics of a multi-rotor MAV and its noise reduction technology," *INTER-NOISE and NOISE-CON Congress and Conference Proceedings*, Vol. 253, Institute of Noise Control Engineering, 2016, pp. 393–403.

[13] Intaratep, N., Alexander, W. N., Devenport, W. J., Grace, S. M., and Dropkin, A., "Experimental study of quadcopter acoustics and performance at static thrust conditions," *22nd AIAA/CEAS Aeroacoustics Conference*, 2016, p. 2873.

[14] de Vries, R., van Arnhem, N., Sinnige, T., Vos, R., and Veldhuis, L. L., "Aerodynamic interaction between propellers of a distributed-propulsion system in forward flight," *Aerospace Science and Technology*, Vol. 118, 2021, p. 107009.

[15] Mayer, Y., Kamliya Jawahar, H., Szoke, M., and Azarpeyvand, M., "Design of an Aeroacoustic Wind Tunnel Facility at the University of Bristol," *2018 AIAA/CEAS Aeroacoustics Conference*, 2018, p. 3138.

[16] Wang, H., Zang, B., Celik, A., Rezgui, D., and Azarpeyvand, M., "An experimental investigation of propeller noise in forward flow," *25th AIAA/CEAS Aeroacoustics Conference*, 2019, p. 2620.

[17] *Axial Force And Torque Transducer*, Novatech, 2015. URL `https://www.novatechloadcells.co.uk/product-pdf/f310`.

[18] *CCP Free-field Array Microphone, High Pressure*, GRAS, 2014. URL `https://www.grasacoustics.com/products/special-microphone/array-microphones/product/ss_export/pdf2?product_id=831`.

[19] *PXI Sound and Vibration Module*, National Instruments, 2017. URL `https://www.ni.com/pdf/manuals/372125f.pdf`.

[20] Tam, C. K. W., "Computational aeroacoustics - Issues and methods," *AIAA Journal*, Vol. 33, No. 10, 1995, pp. 1788–1796. https://doi.org/10.2514/3.12728, URL https://doi.org/10.2514/3.12728.

[21] Singer, B., Lockard, D., and Lilley, G., "Hybrid acoustic predictions," *Computers & Mathematics with Applications*, Vol. 46, No. 4, 2003, pp. 647–669.

[22] Rubio, G., "Numerical methodologies for the determination of noise sources in subsonic flows," Ph.D. thesis, 2007.

[23] Wang, M., Freund, J. B., and Lele, S. K., "Computational prediction of flow-generated sound," *Annu. Rev. Fluid Mech.*, Vol. 38, 2006, pp. 483–512.

[24] Morgans, A. S., Karabasov, S., Dowling, A. P., and Hynes, T., "Transonic helicopter noise," *AIAA journal*, Vol. 43, No. 7, 2005, pp. 1512–1524.

[25] Ffowcs Williams, J. E., and Hawkings, D. L., "Sound generation by turbulence and surfaces in arbitrary motion," *Philosophical Transactions of the Royal Society of London. Series A, Mathematical and Physical Sciences*, Vol. 264, No. 1151, 1969, pp. 321–342.

[26] Curle, N., "The influence of solid boundaries upon aerodynamic sound," *Proceedings of the Royal Society of London. Series A. Mathematical and Physical Sciences*, Vol. 231, No. 1187, 1955, pp. 505–514.

[27] Lighthill, M. J., "On sound generated aerodynamically I. General theory," *Proceedings of the Royal Society of London. Series A. Mathematical and Physical Sciences*, Vol. 211, No. 1107, 1952, pp. 564–587.

[28] Brentner, K. S., and Farassat, F., "Analytical comparison of the acoustic analogy and Kirchhoff formulation for moving surfaces," *AIAA journal*, Vol. 36, No. 8, 1998, pp. 1379–1386.

[29] Farassat, F., and Myers, M., "Extension of Kirchhoff's formula to radiation from moving surfaces," *Journal of Sound and Vibration*, Vol. 123, No. 3, 1988, pp. 451–460.

[30] Welch, P., "The use of fast Fourier transform for the estimation of power spectra: a method based on time averaging over short, modified periodograms," *IEEE Transactions on audio and electroacoustics*, Vol. 15, No. 2, 1967, pp. 70–73.

[31] Mejzlik, "Mejzlik.eu - Design and manufacturing top-quality propellers," , 2022. URL https://www.mejzlik.eu/.

[32] Zore, K., Sasanapuri, B., Parkhi, G., and Varghese, A., "Ansys mosaic poly-hexcore mesh for high-lift aircraft configuration," *21st AeSI Annual CFD Symposium*, 2019.

[33] ANSYS, I., *ANSYS Fluent Meshing User's Guide, Version 15.0*, Canonsburg, PA, 2013. URL https://www.ansys.com/resource-center/brochure/ansys-meshing-solutions-cfd.

[34] ANSYS, I., *ANSYS Fluent User's Guide, Version 19.2*, Canonsburg, PA, 2018. URL https://www.ansys.com/products/fluids/ansys-fluent.

[35] Nicoud, F., and Ducros, F., "Subgrid-scale stress modelling based on the square of the velocity gradient tensor," *Flow, turbulence and Combustion*, Vol. 62, No. 3, 1999, pp. 183–200.

[36] Nardari, C., Casalino, D., Polidoro, F., Coralic, V., Lew, P.-T., and Brodie, J., "Numerical and experimental investigation of flow confinement effects on UAV rotor noise," *25th AIAA/CEAS Aeroacoustics Conference*, 2019, p. 2497.

[37] Glegg, S., and Devenport, W., *Aeroacoustics of low Mach number flows: fundamentals, analysis, and measurement*, Academic Press, 2017.

[38] Weitsman, D., Stephenson, J. H., and Zawodny, N. S., "Effects of flow recirculation on acoustic and dynamic measurements of rotary-wing systems operating in closed anechoic chambers," *The Journal of the Acoustical Society of America*, Vol. 148, No. 3, 2020, pp. 1325–1336.

[39] Thai, A. D., De Paola, E., Di Marco, A., Stoica, L. G., Camussi, R., Tron, R., and Grace, S. M., "Experimental and Computational Aeroacoustic Investigation of Small Rotor Interactions in Hover," *Applied Sciences*, Vol. 11, No. 21, 2021, p. 10016.